Determination of the structure of lithium niobosilicate glasses by molecular dynamics simulation with a new Nb-O potential

Wei Sun[1], Keith Veenhuizen[2], Jacob Marsh[2], Volkmar Dierolf[3], Himanshu Jain[1]*

[1] Department of Materials Science and Engineering, Lehigh University, Bethlehem, PA

[2] Department of Physics, Lebanon Valley College, Annville, PA

[3] Department of Physics, Lehigh University, Bethlehem, PA

*Corresponding author: h.jain@lehigh.edu

Keywords: Lithium niobosilicate glass; Potential development; Molecular dynamics; Glass structure; Raman spectroscopy

Abstract

A partial charge empirical potential for the Nb-O pair has been developed based on existing parameters of other pairs in a Teter potential to enable molecular dynamics simulations of both lithium niobate crystal and lithium niobosilicate glasses. The developed potential is capable of describing structural features of lithium niobosilicate glasses in a wide composition range, including niobium coordination number and bond length, density, bond angle distribution, polyhedral distribution and fraction of bridging oxygen. The results obtained using this new potential show good agreement with experimental data of density and structure from Raman spectroscopy of lithium niobosilicate glasses and X-ray absorption spectroscopy near Nb K-edge.

1. Introduction

Niobium containing glasses find applications in various technologies since the addition of Nb_2O_5 significantly alters their chemical and physical properties, especially the nonlinear optical and electro-optical properties[1–4]. Additionally, lithium niobosilicate glass has been used to fabricate, through continuous wave (CW)[5,6] and femtosecond (*fs*)[7,8] lasers, ferroelectric $LiNbO_3$ crystal architecture that is suitable as optical waveguide within glass owing to its higher refractive index than the matrix. A better understanding of the relationships among composition, structure, and properties is crucial for the development of such applications. Several experimental studies on the structure of Nb_2O_5-containing glasses have been reported in the literature, where the role of Nb and related surrounding structures has raised interests. Ciceo and coworkers[9] pointed out that whether the Nb atoms act as network former or modifier is determined by the ratio between their valence state: Nb^{5+} acts as a glass former while Nb^{4+} acts as a modifier. Generally, Nb^{5+} mainly exists as [NbO_6] octahedra that can create a three-dimensional network with corner- and/or edge-sharing [NbO_6] units. [NbO_4] tetrahedra, though extremely rare, are also found in niobium-containing glasses. Gao et al.[10] reported the existence of four-fold Nb in sodium niobosilicate xNb_2O_5-(1-x/3)(Na_2O • $2SiO_2$) glasses only at very small Nb_2O_5 concentrations (less than 5%). In addition, [NbO_4] tetrahedra have often been observed in rare earth niobate glasses, such as $YNbO_4$, $YbNbO_4$, $LaNbO_4$, and $SmNbO_4$[11,12]. Although significant insights have been gained from these experimental characterizations, the structure of the basic building blocks of niobium containing multi-component glasses and related properties remain unclear.

Atomistic simulations are becoming increasingly more valuable for developing a comprehensive understanding of the structure-property relationship in various materials. Molecular dynamics (MD) simulation is one of the most effective methods to predict atomic-level structure of glasses and amorphous materials, especially to obtain information that is difficult to observe directly from experiments. However, the accuracy of predicted results from MD simulation is sensitively determined by the availability of reliable empirical pairwise potentials. Therefore, the development of effective empirical potentials is a prerequisite, and its applicability must be established by validating simulated structure and properties with experimentally measured values.

For several decades, empirical potentials have been developed and used to study the structures and properties of multi-component glasses such as alkali silicate[13–15], aluminosilicate[16], borosilicate[17,18], and zirconium silicate [19]. However, limited information is available about the potentials for materials containing niobium. Tomlinson et al., and Donnerberg et al. [20–22] proposed an empirical potential for $LiNbO_3$ crystal where the interactions between ions were based on core-shell model. Jackson and Valerio[23] reported another interatomic potential for $LiNbO_3$ crystal which was also validated using core-shell model. All these potentials were developed by reproducing the structure of $LiNbO_3$ crystal only, and have not been tested or validated for establishing amorphous or glass structures. At present, a set of effective empirical potentials has been lacking, which will yield high computational efficiency and is also capable of describing both lithium niobate crystal and niobium containing niobosilicate glasses with high accuracy. For a complete set of potentials containing all the interatomic pairs in multicomponent materials such as lithium niobosilicate glass, a large amount of variables must be considered, where each additional element greatly increases the complexity and adds uncertainty to the force field development process. This complexity has been addressed using the well-established and well-tested Teter potential, which takes into account the partial covalency of bonding in glass network with pair-wise parameters, instead of creating a whole set from scratch. Teter potential was originally developed by D. M. Teter and later modified by Du and Cormack[24] incorporating O-O interactions to improve descriptions of cation-oxygen bond distance and coordination numbers[24]. This potential set has been widely tested with further development and refinement on glasses with a variety of compositions[25–28].

The purpose of this work is to develop and experimentally validate a compatible and effective potential for the Nb-O pair based on reported Teter potential set for simulating the structures of lithium niobate crystal and lithium niobosilicate glasses by using MD simulations. A detailed account of the local environment, especially around Nb, as well as densities and structures were obtained for the (100-x)$LiNbO_3$ – x(SiO_2) (LNSX) glass series as a function of $SiO_2/LiNbO_3$ ratio. Raman spectroscopy and X-ray absorption spectroscopy experiments were performed to provide validation of the structural models from this newly developed potential.

2. Methodology

2.1. Details of empirical potentials

The adopted pairwise potential form for this study is a combination of a long-range Coulomb term and a short-range Buckingham term, with partial effective charge, which is given by following equation:

$$V_{ij}(r_{ij}) = \frac{Z_i Z_j e^2}{4\pi\varepsilon_o r_{ij}} + A_{ij}\exp\left(-\frac{r_{ij}}{\rho_{ij}}\right) - \frac{C}{{r_{ij}}^6} \qquad (1)$$

where Z_i and Z_j are the partial charges of atom i and j to model the partial covalent bonds. e, ε_o, and r_{ij} are the charge of a single electron, vacuum permittivity, and interatomic distance between atom i and j, respectively. The A, ρ, and C are the empirical fitting parameters for the Buckingham term. Additionally, a correction term was introduced to modify the Buckingham potential in order to avoid the unreasonably high energy caused by the power term at short interatomic distances[18]. The correction function at low r_{ij} region is given by:

$$V'_{ij}(r_{ij}) = B_{ij}r_{ij}^{n} - D_{ij}r_{ij}^{2} \quad (2)$$

where *B*, *D*, and *n* are fitted parameters. The function was applied at interatomic distances smaller than a critical value, where the original, first, and second derivative values of the Buckingham term in Equation (1) are equal to those of Equation (2). With the introduction of the splice correction function, the unphysical potential well at short interatomic distances can be avoided. Thus, the system can be simulated at high temperatures required during the melt-quench process.

2.2 Optimization of potential parameters

The parameters for the new potential were optimized by fitting to a set of data from experiments and/or quantum mechanical (QM) calculations, often referred to as the training set. For the Buckingham forcefield, the parameters were optimized by minimizing the "sum of squares" which represents the quality of the fitting process. It is defined as:

$$sum\ of\ squares = \sum_{i=1}^{n} w(X_{i,obs} - X_{i,calc})^2 \quad (3)$$

where $X_{i,obs}$ and $X_{i,calc}$ are the observed and calculated quantities, respectively; n is the total number of data points included in the optimization process; and *w* is the assigned weighting factor for each data. The choice of the weighting factor for each observed data point depends on the relative magnitude of the quantities and the reliability of the data[29].

In this study, the reproduction of structure-related data of lithium niobate crystal and LNS glass is of prime concern. Therefore, the structural information from experiments and Density Functional Theory (DFT) calculations was used to direct the potential parameter development of Nb-related parameters to describe the structure and properties of lithium niobate crystal and LNS glass. For O-O, Si-O, and Li-O pairs in lithium niobate crystal and LNS glass, the parameters were chosen based on existing widely adopted Teter parameterization, which have been extensively used and tested in multicomponent silicate glasses[25–28]. For the Nb-O pair, the same functional form of the effective interatomic potential has been used for establishing the parameters and partial effective charges.

By using General Utility Lattice Program (GULP) program [29], the parameters for the Nb-O pair in the Buckingham potential were initially determined by taking into account the structure of lithium niobate crystal. Accordingly, DFT calculations were performed to obtain a potential training set using geometric optimization, which yielded results consistent with experimental molar volume, lattice energy, and lattice parameters. This step was followed by refinements from MD simulations carried out by DL_POLY package[30] to match the simulated results with experimental structure and properties of lithium niobosilicate series, (100-x)$LiNbO_3$ – x(SiO_2) (LNSX) glasses with varying silica content, x. This procedure is described further in section 2.3. The parameters of existing Li-O, Si-O, and O-O pairs as well as the newly developed Nb-O pair are listed in Table 1.

Table 1. Empirical parameters for Buckingham potential and short-range correction term. All the parameters for Nb-O pair were developed in this work, and those for the other pairs were from previous studies[24–28]

Pairs	A_{ij} (eV)	ρ_{ij} (Å)	C_{ij} (eV•Å^6)	B_{ij}(eV• Å^n)	D_{ij}(eV/ Å^2)	n
$O^{-1.2}-O^{-1.2}$	2029.2204	0.343645	192.580	45.868	-0.333	-3.402
$Si^{2.4}-O^{-1.2}$	13702.9050	0.193817	54.681	28.950	-3.059	-3.932
$Nb^{3.0}-O^{-1.2}$	12897.0060	0.234410	127.710	76.494	-4.060	-3.475
$Li^{0.6}-O^{-1.2}$	41051.9380	0.151160	0.0	-	-	-

2.3 Details of simulations

Calculations of the bulk structure of $LiNbO_3$ crystal were performed using the General Utility Lattice Program (GULP) package[29], following the classical atomistic approach. As a validation of the potentials, the Vienna *ab initio* package (VASP)[31] was used to perform DFT calculations. The energy was calculated using the PAW-PBE[32] generalized gradient approximation (GGA) implanted in the VASP code. The first Brillouin zone was sampled using a 5×5×2 k-point mesh for $LiNbO_3$ crystal. The electronic wave functions were expanded in a plane wave up to a kinetic energy cutoff of 400 eV. A Gaussian smearing of 0.05 eV was applied.

Lithium niobosilicate glasses with different compositions, shown in Table 2, were studied by using MD simulations carried out by DL_POLY package[30], where the density of LNS glasses were taken from experiments reported by Prapitpongwanich *et al.*[33]. The glass systems were generated with ~4000 atoms by randomly placing them in corresponding cells with the densities matching with experiments values[33]. This arrangement was heated to 6000 K using constant volume, number of atoms, and temperature (NVT) ensemble to obtain amorphous melt structure, and then quenched to 300 K gradually with a cooling rate of 5 K/ps. The resulting structure was relaxed at 300 K for 50 ps using a constant pressure, number of atoms, and temperature (NPT) ensemble.

Table 2. Composition (mol%) and density of calculated (100-x)$LiNbO_3$ – x(SiO_2) (LNSX) glasses. The number after the composition name "LNS" denotes to the percentage of SiO_2.

	SiO_2	Nb_2O_5	Li_2O	Density (*g/cm³*)	
				Ref. [33]	**MD**
LNS22	22	39	39	3.970	3.930
LNS26	26	37	37	3.895	3.858
LNS30	30	35	35	3.820	3.809
LNS35	35	32.5	32.5	3.750	3.710
LNS40	40	30	30	3.664	3.645
LNS50	50	25	25	3.451	3.427
LNS60	60	20	20	3.224	3.210

Structural signatures including pair distribution function (PDF), bond angle distribution (BAD), coordination number (CN), and distribution of Q_n (representing number of bridging oxygens around a Si atom) species were adopted to describe the short- and medium-range glass structure. In addition, based on Q_n distribution, the overall network connectivity (NC) was determined from MD simulations, which is defined as:

$$NC = \frac{\sum_{n=0}^{4} n \times Q_n^{Si} \times [\mathrm{SiO_2}] + \sum_{n=0}^{6} n \times Q_n^{Nb} \times [\mathrm{Nb_2O_5}]}{[\mathrm{SiO_2}] + [\mathrm{Nb_2O_5}]} \quad (4)$$

where $\sum_{n=0}^{4} n \times Q_n^{Si}$ and $\sum_{n=0}^{6} n \times Q_n^{Nb}$ are the network connectivity of Si and Nb, respectively, and [SiO_2] and [Nb_2O_5] represent the mole percentage of these two components.

2.4. Experimental Details

Lithium niobosilicate glasses were prepared by mixing appropriate amounts of Li_2CO_3 (99.999%), Nb_2O_5 (99.9985%), and SiO_2 (99.99%) in 40 g batches. Each batch was melted in a Pt-Rh crucible at 1400 °C for one hour, and the melt was quenched by pressing it between two steel plates at room temperature. The glass was subsequently annealed at 500 °C for two hours, and then furnace cooled slowly to room temperature. Raman spectroscopy was performed using a WITec Raman microscope (alpha300 RA) equipped with a 532 nm laser. Peak fitting was performed in the range 550 cm^{-1} - 1200 cm^{-1} to track the shift in energy of the vibrational modes with varying glass composition. For comparison with the simulated Nb – O PDF in glass and crystal, X-ray absorption spectroscopy was performed at the SRX 5-ID beamline at the National Synchrotron Light Source (NSLS-II, Brookhaven National Lab. The extended X-ray absorption fine structure (EXAFS) around the Nb K-edge of LNS30 glass and congruent (lithium deficient) lithium niobate single crystal was measured with a monochromatic X-ray beam in the transmission mode. Plotting and fitting of the EXAFS data was performed using Athena and Artemis software[34]. First shell fitting was performed to extract the Nb – O interatomic distance in glass and crystal.

3. Results

3.1 Structures of $LiNbO_3$ crystals

As mentioned in Section 2, we performed DFT calculations on $LiNbO_3$ crystal to serve as a reference for defining the empirical potential parameters. In order to obtain optimized structure, the equation of states of $LiNbO_3$ crystal from empirical potential were simulated by performing calculations at various constant volume with values ranging ±10% of the experimental value. Then the total energy versus volume curve was plotted and fitted to the Birch equation of state[35], which yielded the equilibrium volume and structure.

Calculated equilibrium lattice parameters for the $LiNbO_3$ crystals compared with DFT and experimental values are included in Table 3. The structural information of the target crystals such as lattice parameters, volume, and mechanical properties are predicted well by using the empirical potential including newly developed parameters for Nb-O pair. These values show a very good match with experiment reference as expected, since they were used for parameterization of the fitting process.

Table 3. Unit cell parameters of $LiNbO_3$ crystal

	This Work		References	
	DFT	MD	DFT[36]	Expt[37]
		Cell parameters		
V($\AA^3$)	329.58 ± 0.02	330.41 ± 0.07	320.56	318.11
a($\AA$)	5.21	5.18	5.21	5.15
c($\AA$)	14.02	14.22	14.12	13.86
α(°)	90	90	90	90
γ(°)	120	120	120	120

3.2 Structure of lithium niobosilicate glasses

3.2.1 Pair distribution function

A series of LNS glasses were simulated by the MD method using the newly developed potential. As a commonly used method to quantitatively describe the short-range bonding structure, the pair distribution function (PDF) was studied, where the first peak gives the distance between two nearest neighbors. The calculated partial pair distributions of all the pairs in LNS35 are shown in Figure 1 as examples. The first main peak of Si-O and Li-O pairs are located at ~1.62 Å and ~1.91 Å, respectively, which are typical of silicate glasses and are in good agreement with reported MD results[15, 36–38] and experimental values[41–43] from X-ray absorption spectra for multicomponent silicate glasses. For Nb-O pair, the PDF shows a narrow and well-defined first peak centered at ~1.95 Å, suggesting a highly ordered local environment of Nb species in glass. Generally, the parameterized potential for the Nb-O pair along with the existing parameters of Si-O, Li-O, and O-O pairs provide reasonable PDF descriptions of lithium niobosilicate glass.

A detailed comparison of the PDFs of LNS glasses and $LiNbO_3$ crystal (if applicable) is shown in Figure 2. For Si-O, Nb-O, and Li-O pairs, shown in Figure 2*a*, *b*, and *c*, respectively, the positions of the main peaks of LNS glasses are in agreement with the EXAFS results for the alkali niobosilicate glasses[10]. No significant changes were observed for Si-O, Nb-O, and Li-O PDFs as a function of SiO_2 concentration. Different from the LNS glasses, the PDFs of $LiNbO_3$ crystal show much higher and sharper peaks for both Nb-O and Li-O pairs, which are centered at smaller distances indicating shorter bonds compared to these two pairs for LNS glasses. The PDF plots of Si-Si, Nb-Nb, and Si-Nb represent the inter-polyhedral connection displayed in Figure 2*d*, *e*, and *f*, respectively. Interestingly, both of the Nb-Nb and Si-Nb PDF results show two peaks at medium range: for the Nb-Nb pair, one is centered around 3.35 Å and the other at 3.85 Å, and for the Si-Nb pair, one is centered around 2.85 Å and the other at 3.45 Å. The peaks at smaller distances are mainly due to edge-sharing [NbO_6]-[NbO_6] octahedra and [NbO_6] octahedra-[SiO_4] tetrahedra, and the peaks with higher intensities at longer bond distances originate from corner-sharing structures. For the Nb-Nb pair, the intensity of the 3.35 Å peaks decreases with increasing silica content, and that of the 3.85 Å peak also decreases slightly. This is due to the concentration of Nb decreasing with increasing SiO_2 content. Additionally, the first main peak of the Nb-Nb PDF from $LiNbO_3$ crystal is located at ~3.61 Å, between the two peaks from LNS glasses. For the Si-Nb pair, the intensity of the peak at ~2.85 Å decreases with increasing silica content, similar to that of the Nb-Nb pair, while the peak at ~3.45 Å increases with increasing silica content.

3.2.2 Bond angle distribution (BAD)

The bond angle distributions are analyzed in this study for the ∠O-T-O angle to describe the regularity of TO_n polyhedral block structure, and the angle formed by ∠T-O-T to describe the polyhedral connectivity, where T stands for Si or Nb species that are considered as glass formers in this glass system. The ∠O-Si-O and ∠O-Nb-O bond angle distributions (BAD) are shown in Figure 3. Although there are small variations of peak intensity, the peak position remains the same for all the LNS glasses. The ∠O-Si-O BAD shows only one peak at ~108°, which is close to the typical tetrahedral angle and agrees well with previously reported MD and experimental results[14]. For the ∠O-Nb-O BAD, shown in Figure 3b, there are two peaks present: one major peak at ~89° and a broader peak with much lower intensity at ~171°, representing the high percentage of six- and five-coordination states of Nb in LNS glasses with distorted octahedral and trigonal bipyramid structures. Similar structures were found in aluminosilicate glasses where six- and five- fold Al atoms were reported[44].

The inter-polyhedral bond angle distributions for ∠Si-O-Si, ∠Nb-O-Nb, and ∠Si-O-Nb are shown in Figure 3*c*, *d*, and *e*, respectively. Combined with the Nb-Nb PDFs, the obtained ∠Nb-O-Nb BADs bring profound insights of how the niobium oxygen polyhedral are connected to each other. In Figure 3*d*, the BAD of ∠Nb-O-Nb has two peaks: one centered at ~102° representing the edge-sharing niobium oxygen polyhedra, and the other at ~141° representing the corner-sharing niobium oxygen polyhedra. Additionally, the trends of intensity of these peaks are consistent with the Nb-Nb PDF results. With increasing silica content, the intensities of the two peaks decrease significantly. While for the ∠Nb-O-Si BAD, shown in Figure 3*e*, the peaks that represent corner-sharing [SiO_4] tetrahedra and [NbO_6] octahedra show increasing intensities and angles with increasing SiO_2 concentration. Taken together with the decreasing intensity of the peak at ~141° in the ∠Nb-O-Nb BAD, we can envisage that a stronger covalent network is formed by corner-sharing niobium and silicon oxygen polyhedra as SiO_2 concentration increases.

3.2.3 Coordination numbers

Coordination numbers (CNs) of Si, Nb, and Li in simulated LNS glasses and $LiNbO_3$ crystal (as applicable) are presented in Table 4. Numbers within the Table represent the percentage of the CN of corresponding species, where the cutoff distances were taken based on the PDF of corresponding pairs. Note that Si remains 100% four coordinated for all the LNS compositions. Nb is mainly six-coordinated but also partially five-coordinated according to our simulated results. When the concentration of SiO_2 increases, the coordination environment around Nb also changes. In the composition with the lowest SiO_2 content, LNS22, 93.44% of the Nb atoms are six-coordinated. This value decreases to 86.25% when the SiO_2 content increases to 60% in LNS60. As a consequence, the average Nb coordination number decreases with the increase of silica content and the decrease of lithium niobate content. This trend is consistent with EXAFS results for the sodium niobosilicate glasses[10], where the average coordination number increases as the Nb_2O_5 concentration increases. For the Li-O pair, the average coordination number at their cutoff distance decreases from 4.08 to 3.77 with a wider distribution as the SiO_2 concentration increases, indicating a behavior characteristic of the network modifier.

Table 4. Coordination number distribution of Si, Nb, and Li cations for LNS glasses

			Si-O			
	2	3	4	5	6	AVG
LNS22			100			4.00
LNS26			100			4.00
LNS30			100			4.00

LNS40			100			4.00
LNS50			100			4.00
LNS60			100			4.00
			Nb-O			
	2	3	4	5	6	AVG
LNS22				6.56 ± 0.55	93.44 ± 0.55	5.93
LNS26				7.17 ± 0.71	92.84 ± 0.71	5.92
LNS30				8.17 ± 0.75	91.83 ± 0.75	5.91
LNS40				9.33 ± 0.71	90.67 ± 0.71	5.90
LNS50				9.76 ± 0.52	90.24 ± 0.52	5.90
LNS60				13.80 ± 0.87	86.25 ± 0.87	5.86
			Li-O			
	2	3	4	5	6	AVG
LNS22	0.68 ± 0.15	21.28 ± 1.35	50.09 ± 2.38	24.66 ± 0.98	3.29 ± 0.74	4.08
LNS26	1.40 ± 0.81	21.80 ± 1.80	51.84 ± 1.09	22.61 ± 1.09	2.35 ± 0.20	4.03
LNS30	1.33 ± 0.58	22.43 ± 1.62	51.76 ± 0.65	22.24 ± 0.95	2.24 ± 0.36	4.01
LNS40	1.61 ± 0.38	24.72 ± 1.94	50.72 ± 1.34	20.78 ± 1.88	2.17 ± 0.17	3.97
LNS50	2.40 ± 0.72	26.67 ± 2.37	51.07 ± 2.00	18.47 ± 2.39	1.40 ± 0.35	3.90
LNS60	4.00 ± 1.15	30.83 ± 1.88	49.50 ± 2.18	15.00 ± 0.66	0.67 ± 0.14	3.77

3.2.4 Glass network structure

The Q_n in glass represents the number (*n*) of bridging oxygen connecting with network-former species (Q), the distribution of which provides information about medium range order how the network former units connect with each other. Specifically, we assume in lithium niobosilicate glasses that SiO_2 and Nb_2O_5 are both considered as network formers according to experimental and simulated results (see the Discussion section for more details), therefore all the linkages connecting the structural units formed by these two network former species are taken into consideration. That is, the oxygen atoms in Si-O-Si, Si-O-Nb, and Nb-O-Nb linkages are considered as bridges for this network, and those bonded to Li (e.g. Li-O-Si/Nb) are considered non-bridging oxygens.

Percentages of Q_n units of Si and Nb in simulated LNS glasses are plotted in Figure 4. For LNS22 glass, containing the lowest SiO_2 content, Q_3 and Q_4 species of Si (Figure 4a) are ~15.4% and 84.0%, respectively. With the increase of SiO_2 concentration, Q_4 of Si increases to over 90%, while Q_3 decreases below 10%, which indicates a polymerization of glass structure at the higher $SiO_2/LiNbO_3$ ratio. The Q_n species of Nb are mainly in Q_6 structure in LNS22 (77.8%) with a minor part in Q_5 (20.4%) and very small amount in Q_4 (1.8%) species, as shown in Figure 4b. The percentage of Q_6 decreases slightly as the SiO_2 increasing. No Q_1, Q_2, and Q_3 species of Nb were observed in these compositions. Based on the above calculated results of Q_n distributions, we take the next step and calculate the corresponding network connectivity (NC) according to Equation (3). Table 5 indicates that the NC of Si increases from 3.79 to 3.90 with the increase of SiO_2 concentration, while the NC of Nb is unaffected by the composition change. Interestingly, the overall network connectivity is found to decrease noticeably from 5.34 to 4.63 from LNS22 to LNS60. This is due to the large amount of Q_6 of Nb, which contributes greatly to the overall NC based on Eq. (4).

Table 5. Network connectivity (NC) of Si, Nb, and the overall and percentages of BO, NBO, and TBO in simulated LNS glasses. Number without errors have a standard deviation less than 0.01

	Network Connectivity			Oxygen coordination (%)		
	Si	Nb	All	NBO	BO	TBO
LNS22	3.79	5.77	5.34	6.25 ± 0.29	88.86 ± 0.38	4.83 ± 0.16
LNS26	3.78	5.80	5.28	5.95 ± 0.41	89.72 ± 0.74	4.32 ± 0.34
LNS30	3.84	5.78	5.20	5.86 ± 0.31	89.73 ± 0.30	4.17 ± 0.34
LNS40	3.84	5.81	5.02	5.52 ± 0.15	90.94 ± 0.33	3.50 ± 0.20
LNS50	3.86	5.80	4.83	4.82 ± 0.30	92.16 ± 0.56	3.01 ± 0.26
LNS60	3.90	5.73	4.63	4.26 ± 0.32	93.78 ± 0.53	1.94 ± 0.23

In addition to the NC, percentages of bridging oxygen (BO) and non-bridging oxygen (NBO) in simulated glasses are shown in Table 5. The overall percentage of BO increases and NBO decreases with higher $SiO_2/LiNbO_3$ ratio. This trend can be attributed to the decreasing Li concentration resulting in fewer network modifiers within the glass network to break the BO bonds. $SiO_2/LiNbO_3$ substitution has therefore essentially polymerized the silicon/niobium oxygen network. It is worth mentioning that a small percentage of tri-bridging oxygen (TBO), namely three-fold coordinated oxygen atoms are observed in all the simulated LNS glasses and their concentration is listed in Table 5 as well. The percentage of TBO decreases as the $SiO_2/LiNbO_3$ ratio increases.

Polyhedral connectivity between [SiO_4] and [NbO_6] was calculated to characterize medium-range structure of LNS glasses. Table 6 shows the percentages of corner-shared [NbO_6]-[NbO_6] and [NbO_6]-[SiO_4] in LNS glasses. Note that linkages between [SiO_4] tetrahedra are completely corner-sharing for all the calculated compositions, so only the other two linkages are listed in Table 6. The linkages between [NbO_6] octahedra and [SiO_4] tetrahedra are mostly corner-sharing, higher than 99%, with the edge-shared [NbO_6]-[SiO_4] less than 1% for all the LNS compositions; the increase of SiO_2 concentration has limited effect on this type of connection. However, the interconnection between two [NbO_6] octahedra are more sensitive to the composition change, though the dominant type of connection is still corner-sharing. The corner-shared [NbO_6]-[NbO_6] in LNS22 accounts for 93.2% of the total connected units, while the edge-sharing accounts for 6.8%. From LNS22 to LNS60 with the SiO_2 concentration increasing, the percentage of corner-shared [NbO_6]-[NbO_6] octahedra increase from 93.2% to 95.5%, corresponding to the decreased intensities of Nb-O-Nb BAD at around 105° in Figure 3d.

Table 6. Percentages of corner- and edge shared [NbO_6]-[SiO_4] and [NbO_6]- [NbO_6] linkages

	[NbO_6]-[SiO_4]		[NbO_6]- [NbO_6]	
	Corner	Edge	Corner	Edge
LNS22	99.53	0.48	93.20	6.80
LNS26	99.28	0.73	93.38	6.62
LNS30	99.35	0.65	94.25	5.75
LNS40	99.28	0.72	94.78	5.23
LNS50	99.50	0.50	95.05	4.95
LNS60	99.33	0.67	95.45	4.55

3.3 Experimental results

3.3.1. Raman spectroscopy of lithium niobosilicate glasses

The Raman spectra of lithium niobosilicate glasses of LNS22, LNS26, LNS30, and LNS34 compositions are shown in Figure 5. Assignments of the vibrational modes at different energies to structural units in niobosilicate glasses have been reported in the literature[10,45]. Focusing specifically on those modes above 550 cm^{-1}, the band around 650 cm^{-1} corresponds to stretching vibration of the Nb-O bond that is less distorted or is without non-bridging oxygen, the band around 800 cm^{-1} corresponds to short vibration of Nb-O in [NbO_6] octahedra with non-bridging oxygen or severe distortion caused by overwhelming concentration of [NbO_6] octahedra, the band around 870 cm^{-1} corresponds to vibration of Nb with neighboring non-bridging oxygen, and the band around 1000 cm^{-1} corresponds to vibrations of [SiO_4] tetrahedra.

It is apparent from the spectra in Figure 5 that with increasing SiO_2 concentration, the 650 cm^{-1} band increases in frequency while the 800 cm^{-1} band decreases in frequency. Also, as expected, the relative height of the 1000 cm^{-1} band increases with increasing SiO_2 concentration since it is attributed to vibrations of [SiO_4] tetrahedra. To quantify the shift of the 650 cm^{-1} and 800 cm^{-1} bands with varying SiO_2 concentration, peak fitting was performed in the range 550 – 1200 cm^{-1} using four Lorentzian peaks (one for each mode listed above). The locations of the 650 cm^{-1} and 800 cm^{-1} peaks as a function of composition are shown in the inset in figure 5. With increasing SiO_2 concentration, the 650 cm^{-1} band increases by 2.5 cm^{-1} and the 800 cm^{-1} band decreases by 3 cm^{-1}.

3.3.2. EXAFS of lithium niobosilicate glass and lithium niobate crystal

The Nb K-edge EXAFS spectra for LNS30 glass and congruent lithium niobate single crystal are shown in Figure 6. Note that the PDFs determined from EXAFS analysis in real space do not give the absolute, but only relative, values of interatomic distances [46]. Comparison of the EXAFS data for crystal and glass in real space PDF shows that the first peak for crystal occurs at ~1.14 Å, whereas the first peak for glass occurs at slightly higher radial distance, ~1.17 Å. This trend agrees with the Nb–O PDF simulation data shown in Figure 2. The first peak in real space PDF from EXAFS corresponds to single scattering events of photoelectrons from the oxygen nearest neighbors. Fitting of the first shell was performed using Artemis data analysis package, yielding a Nb–O interatomic distance in lithium niobate crystal and LNS 30 glass of 1.856 ± 0.015 Å and 1.894 ± 0.013 Å, respectively. The real space EXAFS is generated by a Fourier transform of the k-space EXAFS. The oscillation in k-space possesses a phase shift, which is why the peaks in Figure 6 appear at lower radial distances (1.14 Å for crystal, 1.17 Å for glass) compared to the MD simulated radial distances. Artemis determines the phase-corrected values of radial distances from EXAFS as 1.856 Å for crystal, and 1.894 Å for glass.

4. Discussion

Experimentally, the structural role of Nb_2O_5 in glasses has been widely studied and discussed. It is well accepted that Nb_2O_5 acts as a network former in the backbone network along with other formers, such as Si and P to polymerize the glass network[8, 43–46]. By using MD simulation with newly developed potentials, the role of Nb_2O_5 in lithium niobosilicate glasses has been studied in much greater detail in this work by analyzing the local structure around Nb from various perspectives. According to the random network theory proposed by Zachariasen[51], the cation must bond with surrounding oxygens to form tetrahedra or octahedra that share corners with each other in order to form the three-dimensional glass network. The structural features of network former in short- and medium-range are well captured by the present MD simulations. First, the well-defined Nb-O pair distribution function in Figure 2 and the stable coordination distribution in Table 4 indicate a definitive first coordination shell of Nb with mostly six-fold coordination and small fraction in five-fold coordination. This result is consistent with the experimental finding that the four-fold niobium units[10], $[NbO_4]$, are extremely rare because Nb^{5+} ion is too large to fit in an oxygen tetrahedron cage. Secondly, the Nb-O-Nb and Nb-O-Si bond angle distribution show peaks with high intensity at around 140°, suggesting large amount of corner sharing $[NbO_6]$-$[NbO_6]$ and $[NbO_6]$-$[SiO_4]$. This observation is further confirmed in Table 6, where a substantial number (over 90%) of corner-shared polyhedra that contain Nb^{5+} are observed in all the simulated LNS compositions.

Another classification criterion proposed by Dietzel[52] to differentiate between network formers and modifiers in oxide glass is the field strength with the value of Z/a^2, where Z and a denote to the ionic charge and ionic radius of both cation and oxygen, respectively. In this theory, network formers are the cations having field strengths higher than 1.2, while network modifiers are found with much lower field strengths, less than 0.5, and network intermediates have field strengths in between. In LNS glasses, Nb^{5+}, which has field strength of 1.27, can be defined as a former ion, consistent with the MD results in this study.

The coordination number of Nb is affected dramatically by the $SiO_2/LiNbO_3$ substitution. The Nb^{5+} ion was reported as mainly existing in [NbO_6] octahedra in silicate glasses. Note that the [NbO_4] tetrahedra were also reported to exist in the amorphous matrix of silicate glasses. Gao et al.[10] reported the existence of [NbO_4] units in sodium niobosilicate glasses, but only for Nb_2O_5 concentration less than 5 mol% and with SiO_2 concentration higher than 63.3 mol%. However, for Nb_2O_5 higher than 20 mol%, only [NbO_6] octahedra are shown to exist in the glass network[10]. Our Raman results show two peaks related to Nb-O vibrations, presumably related to vibrations of [NbO_6] octahedra, as shown in Figure 5. Note that the [NbO_5] unit has a pyramid-shaped structure that can be considered as part of [NbO_6] octahedron, as illustrated in Figure 7. From MD results, the Nb species are found to exist with coordination numbers five and six, but not as four-coordinated [NbO_4] units, which supports the experimental observations. In addition, the six coordinated Nb decreases while five coordinated Nb increases with $SiO_2/LiNbO_3$ substitution. In LNS glasses, the six-fold coordinated $[NbO_6]^{1-}$ bears a negative charge and hence requires a charge compensator, which is Li^+ in this system. As the SiO_2 concentration increases, the Li_2O as well as the Nb_2O_5 concentration decreases. Therefore, fewer Li^{1+} ions are available to compensate the negative charge, which in turn would result in the increased number of [NbO_5] units. To further confirm this inference, the effect of Li_2O content on Nb coordination number was investigated by simulating glass series $y Li_2O \cdot (1-y)/4[3SiO_2 \cdot Nb_2O_5]$ glasses with y = 0.16, 0.20, 0.28, and 0.44. The SiO_2/Nb_2O_5 ratio was kept at 3 which is the ratio of LNS60 that shows the highest amount of five-coordinated Nb. The calculated Nb coordination numbers are listed in Table 7. Our simulation results show that with low Li_2O content (y=0.16) in in this series, the five-fold Nb increases to 34.3% compared to that in LNS60. However, as the concentration of Li_2O increases to y=0.28, the percentage of six-fold Nb increases pronouncedly in accordance with decreasing percentage of five-fold Nb, meaning that with sufficient Li ions as charge compensator, the Nb ions are dominantly six-fold coordinated.

Table 7. Coordination number distribution (%) of Nb polyhedra in $yLi_2O \cdot (1-y)/4[3SiO_2 \cdot Nb_2O_5]$ glasses

y	5	6
0.16	34.2 ± 0.48	65.8 ± 0.48
0.20	13.7 ± 0.59	86.3 ± 0.59
0.28	0.2 ± 0.25	99.8 ± 0.25

0.44	0.0	100

The pair distribution function representing the bond distance for LNS glasses are studied. The main peaks in these PDFs peaks are in good agreement with previous experimental results. Notably, the Nb-O pair shows different bond distances in $LiNbO_3$ crystal and LNS glass. The PDFs of Nb-O pair in the simulated structures are illustrated in Figure 2b, where the Nb-O bond distance in LNS glass is larger than that in crystal. The simulated results are validated qualitatively by our EXAFS data shown in Figure 6, where the bond distances of $LiNbO_3$ crystal and LNS30 glass from real space show the same trend.

From our Raman spectroscopy results, the increase of SiO_2 in LNS glasses results in less distorted [NbO_6] octahedra. This is evidenced by the Nb-O bond vibration at around 800 cm^{-1}, which represents the distorted [NbO_6] with NBOs, shifting to lower frequencies, shown in the inset of Figure 5. This observation is consistent with MD simulated results using newly developed empirical potential where local structure in short- and medium-range around Nb shows distinct features with the SiO_2/$LiNbO_3$ substitution. With increase of SiO_2, the two main peaks of O-Nb-O (Figure 3b) shift to higher angles and the intensities of BAD peaks of Nb-O-Nb (Figure 3d) decrease markedly, especially for the peak at ~104° that represents corner-sharing [NbO_6]-[NbO_6] octahedra. The change of BADs indicates less distorted [NbO_6] octahedra with the addition of SiO_2, which is further confirmed by the increased concentration of corner-shared [NbO_6]-[NbO_6] linkages shown in Table 6.

It is worth mentioning that the presence of tri-bridging oxygen clusters in LNS glass can be attributed to the formation of edge-sharing [NbO_6]-[NbO_6] octahedra structures. As demonstrated in Figure 7, the edge-sharing octahedra create extra space for the oxygen to bond with another Nb atom. Therefore, the percentage of TBO decreases notably as the concentration of edge-sharing structures decreases, as shown in Table 6. Similar structure was reported by Tossel and Horbach[53] in aluminum silicate glasses, where tri-cluster O was coordinated to three Al atoms and formed part of a shared edge.

Another Nb-O vibration observed via Raman spectroscopy in Figure 5 is located at around 650 cm^{-1}. It stands for Nb-O vibration where the O atoms are all bridging oxygen. The peak shifts to higher frequency when the SiO_2 content increases. This observation can be explained by MD simulation results: as the ratio of $SiO_2/LiNbO_3$ content increases, the number of Nb-O-Si linkages increases while the number of Nb-O-Nb linkages decreases, meanwhile the bridging O around Nb more likely bonds with Si with increasing SiO_2. Since the Si-O bonds are stronger than those of Nb-O, as predicted by field strength calculations, the energy of Nb-O at 650 cm^{-1} increases, as observed.

5. Conclusion

In this study, we developed a set of partial charge pairwise potentials for Nb-O to simulate the structure of niobium containing multi-component oxide glasses and $LiNbO_3$ crystal. Combining with Li-O, Si-O, and O-O pairs from published Teter potential, a series of lithium niobosilicate glasses with compositions of $(1-x)LiNbO_3 \cdot xSiO_2$ (mol%) were simulated using MD calculations. It was found that the newly developed parameters are capable to reproduce the structure and density of LNS glasses in a wide composition range. The calculated density, Nb-O bond distance, Nb coordination numbers are consistent with experimental results. The increase of five-fold Nb with the addition of SiO_2 concentration is due to the insufficient Li to balance the charge. No four-fold Nb was observed. The well-defined first coordination shell, large concentration of corner-shared $[NbO_6]$-$[NbO_6]$ and $[NbO_6]$-$[SiO_4]$ structures, as well as high field strength suggest the network former role of Nb ions in LNS glasses. It was found that increase of $SiO_2/LiNbO_3$ ratio results in higher ∠Nb-O-Nb bond angles and lower concentration of edge-shared $[NbO_6]$-$[NbO_6]$ octahedra, indicating less distorted $[NbO_5]$ tetrahedra in glass network, which is consistent with the peak shifting in our Raman spectroscopy results. Detailed information has been organized and drafted, and submitted to *Computational Materials Science*.

6. Acknowledgments

This work was supported by the Basic Energy Sciences Division of the Department of Energy under project DE-SC0005010. Calculations were carried out in the Extreme Science and Engineering Discovery Environment (XSEDE) supported by National Science Foundation

Award 1548562, and in Lehigh University's Research Computing infrastructure partially supported by National Science Foundation Award 2019035.Part of this research used beamline SRX 5-ID of the National Synchrotron Light Source II, a U.S. Department of Energy (DOE) Office of Science User Facility operated for the DOE Office of Science by Brookhaven National Laboratory under Contract No. DE-SC0012704.

Figures captions:

Figure 1. Pair distribution functions of simulated LNS35 glass.

Figure 2. Pair distribution function of (*a*) Si-O, (*b*) Nb-O, (*c*) Li-O, (*d*) Si-Si, (*e*) Nb-Nb, and (*f*) Nb-Si pairs in simulated $LiNbO_3$ crystal (if applicable) and LNS glasses.

Figure 3. Bond angle distributions of (*a*) O-Si-O, (*b*) O-Nb-O, (*c*) Si-O-Si, (*d*) Nb-O-Nb and (*e*) Si-O-Nb in simulated LNS glasses.

Figure 4. Q_n distribution of (*a*) Si and (*b*) Nb in simulated LNS glasses.

Figure 5. Raman spectra of LNS glasses. Gray region indicates the range in which fitting was performed.

Figure 6. Nb K-edge EXAFS spectra of LNS30 glass: (*a*) E-space, (*b*) k-space, and (*c*) real space.

Figure 7. Schematic structures of simulated LNS22 glass (right), [NbO5] structure (top left), and TBO with edge-sharing [NbO6]-[NbO6] linkages (bottom left).

Reference

[1] R.C. Miller, A. Savage, TEMPERATURE DEPENDENCE OF THE OPTICAL PROPERTIES OF FERROELECTRIC LiNbO3 AND LiTaO3, Appl. Phys. Lett. 9 (1966) 169–171. https://doi.org/10.1063/1.1754695.

[2] E.M. Vogel, S.G. Kosinski, D.M. Krol, J.L. Jackel, S.R. Friberg, M.K. Oliver, J.D. Powers, Structural and optical study of silicate glasses for nonlinear optical devices, J. Non. Cryst. Solids. 107 (1989) 244–250. https://doi.org/https://doi.org/10.1016/0022-3093(89)90469-9.

[3] B. Samuneva, S. Kralchev, V. Dimitrov, Structure and optical properties of niobium silicate glasses, J. Non. Cryst. Solids. 129 (1991) 54–63. https://doi.org/https://doi.org/10.1016/0022-3093(91)90080-P.

[4] V. Nazabal, E. Fargin, J.J. Videau, G. Le Flem, A. Le Calvez, S. Montant, E. Freysz, A. Ducasse, M. Couzi, Second-Harmonic Generation of Electrically Poled Borophosphate Glasses: Effects of Introducing Niobium or Sodium Oxides, J. Solid State Chem. 133 (1997) 529–535. https://doi.org/https://doi.org/10.1006/jssc.1997.7527.

[5] T. Komatsu, K. Koshiba, T. Honma, Preferential growth orientation of laser-patterned LiNbO3 crystals in lithium niobium silicate glass, J. Solid State Chem. 184 (2011) 411–418. https://doi.org/https://doi.org/10.1016/j.jssc.2010.12.016.

[6] T. Honma, T. Komatsu, Patterning of two-dimensional planar lithium niobate architectures on glass surface by laser scanning, Opt. Express. 18 (2010) 8019–8024. https://doi.org/10.1364/OE.18.008019.

[7] K. Veenhuizen, S. McAnany, R. Vasudevan, D. Nolan, B. Aitken, S. Jesse, S. V Kalinin, H. Jain, V. Dierolf, Ferroelectric domain engineering of lithium niobate single crystal confined in glass, MRS Commun. 9 (2019) 334–339. https://doi.org/10.1557/mrc.2018.234.

[8] K. Veenhuizen, S. McAnany, D. Nolan, B. Aitken, V. Dierolf, H. Jain, Fabrication of graded index single crystal in glass, Sci. Rep. 7 (2017) 44327. https://doi.org/10.1038/srep44327.

[9] R.L. Ciceo, M. Todea, D. Toloman, M. Muresan-Pop, V. Simon, Structure-composition correlation in niobium containing borophosphate glasses, J. Non. Cryst. Solids. 542 (2020) 120102. https://doi.org/https://doi.org/10.1016/j.jnoncrysol.2020.120102.

[10] G. Huanxin, W. Zhongcai, W. Shizhuo, Properties and structure of niobosilicate glasses, J. Non. Cryst. Solids. 112 (1989) 332–335. https://doi.org/https://doi.org/10.1016/0022-3093(89)90548-6.

[11] J.M. Jehng, I.E. Wachs, Structural chemistry and Raman spectra of niobium oxides, Chem. Mater. 3 (1991) 100–107. https://doi.org/10.1021/cm00013a025.

[12] A.K. Pradhan, R.N.P. Choudhary, Vibrational Spectra of Rare Earth Orthoniobates, Phys. Status Solidi. 143 (1987) K161–K166. https://doi.org/https://doi.org/10.1002/pssb.2221430256.

[13] W. Sun, V. Dierolf, H. Jain, Molecular dynamics simulation of the effect of cooling rate on the structure and properties of lithium disilicate glass, J. Non. Cryst. Solids. 569 (2021) 120991. https://doi.org/https://doi.org/10.1016/j.jnoncrysol.2021.120991.

[14] J. Du, A.N. Cormack, The medium range structure of sodium silicate glasses: a molecular dynamics simulation, J. Non. Cryst. Solids. 349 (2004) 66–79. https://doi.org/http://dx.doi.org/10.1016/j.jnoncrysol.2004.08.264.

[15] J. Du, L.R. Corrales, Structure, dynamics, and electronic properties of lithium disilicate melt and glass, J. Chem. Phys. 125 (2006). https://doi.org/10.1063/1.2345060.

[16] Y. Xiang, J. Du, M.M. Smedskjaer, J.C. Mauro, Structure and properties of sodium aluminosilicate glasses from molecular dynamics simulations, J. Chem. Phys. 139 (2013) 44507. https://doi.org/10.1063/1.4816378.

[17] L. Deng, J. Du, Development of effective empirical potentials for molecular dynamics simulations of the structures and properties of boroaluminosilicate glasses, J. Non. Cryst. Solids. 453 (2016) 177–194. https://doi.org/10.1016/j.jnoncrysol.2016.09.021.

[18] L. Deng, J. Du, Development of boron oxide potentials for computer simulations of multicomponent oxide glasses, J. Am. Ceram. Soc. 102 (2019) 2482–2505. https://doi.org/10.1111/jace.16082.

[19] X. Lu, L. Deng, J. Du, Effect of ZrO2 on the structure and properties of soda-lime silicate glasses from molecular dynamics simulations, J. Non. Cryst. Solids. 491 (2018) 141–150. https://doi.org/https://doi.org/10.1016/j.jnoncrysol.2018.04.013.

[20] H. Donnerberg, S.M. Tomlinson, C.R.A. Catlow, O.F. Schirmer, Computer-simulation studies of intrinsic defects in ${\mathrm{LiNbO}}_{3}$ crystals, Phys. Rev. B. 40 (1989) 11909–11916. https://doi.org/10.1103/PhysRevB.40.11909.

[21] S.M. Tomlinson, C.M. Freeman, C.R.A. Catlow, H. Donnerberg, M. Leslie, Atomistic simulation studies of technologically important oxides, J. Chem. Soc.{,} Faraday Trans. 2.

85 (1989) 367–383. https://doi.org/10.1039/F29898500367.

[22] S.M. Tomlinson, C.R.A. Catlow, H. Donnerberg, M. Leslie, Deriving an Empirical Potential for Ferroelectric LiNbO3, Mol. Simul. 4 (1990) 335–339. https://doi.org/10.1080/08927029008022396.

[23] R.A. Jackson, M.E.G. Valerio, A new interatomic potential for the ferroelectric and paraelectric phases of {LiNbO}3, 17 (2005) 837–843. https://doi.org/10.1088/0953-8984/17/6/005.

[24] J. Du, A.N. Cormack, Molecular Dynamics Simulation of the Structure and Hydroxylation of Silica Glass Surfaces, J. Am. Ceram. Soc. 88 (2005) 2532–2539. https://doi.org/10.1111/j.1551-2916.2005.00352.x.

[25] J. Du, Y. Xiang, Effect of strontium substitution on the structure, ionic diffusion and dynamic properties of 45S5 Bioactive glasses, J. Non. Cryst. Solids. 358 (2012) 1059–1071. https://doi.org/https://doi.org/10.1016/j.jnoncrysol.2011.12.114.

[26] J. Du, L. Kokou, Europium environment and clustering in europium doped silica and sodium silicate glasses, J. Non. Cryst. Solids. 357 (2011) 2235–2240. https://doi.org/https://doi.org/10.1016/j.jnoncrysol.2010.11.088.

[27] L. Deng, J. Du, Erratum: "Development of boron oxide potentials for computer simulations of multicomponent oxide glasses" [J. Am. Ceram. Soc. 102 [5] 2482-2505 (2019)], J. Am. Ceram. Soc. 103 (2020) 2933. https://doi.org/10.1111/jace.16897.

[28] W. Sun, V. Dierolf, H. Jain, Effects of Surface Orientation and Termination Plane on Glass-to-Crystal Transformation of Lithium Disilicate by Molecular Dynamics Simulations, Phys. Status Solidi. n/a (2020) 2000427. https://doi.org/https://doi.org/10.1002/pssb.202000427.

[29] J.D. Gale, GULP: A computer program for the symmetry-adapted simulation of solids, J. Chem. Soc.{,} Faraday Trans. 93 (1997) 629–637. https://doi.org/10.1039/A606455H.

[30] W. Smith, T.R. Forester, DL_POLY_2.0: A general-purpose parallel molecular dynamics simulation package, J. Mol. Graph. 14 (1996) 136–141. https://doi.org/https://doi.org/10.1016/S0263-7855(96)00043-4.

[31] G. Kresse, J. Hafner, Ab initio molecular dynamics for liquid metals, Phys. Rev. B. 47 (1993) 558–561. https://doi.org/10.1103/PhysRevB.47.558.

[32] J.P. Perdew, K. Burke, M. Ernzerhof, Generalized Gradient Approximation Made Simple, Phys. Rev. Lett. 77 (1996) 3865–3868. https://doi.org/10.1103/PhysRevLett.77.3865.

[33] P. Prapitpongwanich, K. Pengpat, C. Rüssel, Phase separation and crystallization in LiNbO3/SiO2 glasses, Mater. Chem. Phys. 113 (2009) 913–918. https://doi.org/https://doi.org/10.1016/j.matchemphys.2008.08.070.

[34] B. Ravel, M. Newville, {\it ATHENA}, {\it ARTEMIS}, {\it HEPHAESTUS}: data analysis for X-ray absorption spectroscopy using {\it IFEFFIT}, J. Synchrotron Radiat. 12 (2005) 537–541. https://doi.org/10.1107/S0909049505012719.

[35] F. Birch, Finite Elastic Strain of Cubic Crystals, Phys. Rev. 71 (1947) 809–824. https://doi.org/10.1103/PhysRev.71.809.

[36] K. Toyoura, M. Ohta, A. Nakamura, K. Matsunaga, First-principles study on phase transition and ferroelectricity in lithium niobate and tantalate, J. Appl. Phys. 118 (2015) 64103. https://doi.org/10.1063/1.4928461.

[37] R. Hsu, E.N. Maslen, D. du Boulay, N. Ishizawa, Synchrotron X-ray Studies of LiNbO${\sb 3}$ and LiTaO${\sb 3}$, Acta Crystallogr. Sect. B. 53 (1997) 420–428. https://doi.org/10.1107/S010876819600777X.

[38] J. Du, L.R. Corrales, Structure, dynamics, and electronic properties of lithium disilicate melt and glass, J. Chem. Phys. 125 (2006) 114702. https://doi.org/10.1063/1.2345060.

[39] D.M. Zirl, S.H. Garofalini, Structure of Sodium Aluminosilicate Glasses, J. Am. Ceram. Soc. 73 (n.d.) 2848–2856. https://doi.org/10.1111/j.1151-2916.1990.tb06685.x.

[40] M. Collin, M. Fournier, P. Frugier, T. Charpentier, M. Moskura, L. Deng, M. Ren, J. Du, S. Gin, Structure of International Simple Glass and properties of passivating layer formed in circumneutral pH conditions, 2 (2018).

[41] G.N. Greaves, A. Fontaine, P. Lagarde, D. Raoux, S.J. Gurman, Local structure of silicate glasses, Nature. 293 (1981) 611. http://dx.doi.org/10.1038/293611a0.

[42] J. Zhao, P.H. Gaskell, M.M. Cluckie, A.K. Soper, A neutron diffraction, isotopic substitution study of the structure of Li2O·2SiO2 glass, J. Non. Cryst. Solids. 232–234 (1998) 721–727. https://doi.org/https://doi.org/10.1016/S0022-3093(98)00554-7.

[43] A.C. Hannon, B. Vessal, J.M. Parker, The structure of alkali silicate glasses, J. Non. Cryst. Solids. 150 (1992) 97–102. https://doi.org/https://doi.org/10.1016/0022-3093(92)90102-P.

[44] J. Du, Molecular Dynamics Simulations of the Structure and Properties of Low Silica Yttrium Aluminosilicate Glasses, J. Am. Ceram. Soc. 92 (2009) 87–95. https://doi.org/10.1111/j.1551-2916.2008.02853.x.

[45] B. Yu, B. Chen, X. Yang, J. Qiu, X. Jiang, C. Zhu, K. Hirao, Study of crystal formation in borate, niobate, and titanate glasses irradiated by femtosecond laser pulses, J. Opt. Soc. Am. B. 21 (2004) 83–87. https://doi.org/10.1364/JOSAB.21.000083.

[46] S. Calvin, XAFS for Everyone, CRC press, 2013.

[47] L. Ghussn, R.M.C.V. Reis, R.K. Brow, D.B. Baker, Color bleaching and oxygen diffusion in a niobium phosphate glass, J. Non. Cryst. Solids. 401 (2014) 96–100. https://doi.org/https://doi.org/10.1016/j.jnoncrysol.2013.11.004.

[48] C.M. Chu, J.J. Wu, S.W. Yung, T.S. Chin, T. Zhang, F.B. Wu, Optical and structural properties of Sr–Nb–phosphate glasses, J. Non. Cryst. Solids. 357 (2011) 939–945. https://doi.org/https://doi.org/10.1016/j.jnoncrysol.2010.12.009.

[49] I.O. Mazali, L.C. Barbosa, O.L. Alves, Preparation and characterization of new niobophosphate glasses in the Li2O-Nb2O5-CaO-P2O5 system, J. Mater. Sci. 39 (2004) 1987–1995. https://doi.org/10.1023/B:JMSC.0000017760.85512.60.

[50] S.M. Hsu, J.J. Wu, S.W. Yung, T.S. Chin, T. Zhang, Y.M. Lee, C.M. Chu, J.Y. Ding, Evaluation of chemical durability, thermal properties and structure characteristics of Nb–Sr-phosphate glasses by Raman and NMR spectroscopy, J. Non. Cryst. Solids. 358 (2012) 14–19. https://doi.org/https://doi.org/10.1016/j.jnoncrysol.2011.08.006.

[51] W.H. Zachariasen, The atomic arrangement in glass, J. Am. Chem. Soc. 54 (1932) 3841–3851. https://doi.org/10.1021/ja01349a006.

[52] A. Dietzel, Die Kationenfeldstärken und ihre Beziehungen zu Entglasungsvorgängen, zur Verbindungsbildung und zu den Schmelzpunkten von Silicaten, Zeitschrift Für Elektrochemie Und Angew. Phys. Chemie. 48 (1942) 9–23. https://doi.org/https://doi.org/10.1002/bbpc.19420480104.

[53] J.A. Tossell, J. Horbach, O Triclusters Revisited: Classical MD and Quantum Cluster Results for Glasses of Composition (Al2O3)2(SiO2), J. Phys. Chem. B. 109 (2005) 1794–1797. https://doi.org/10.1021/jp0454873.

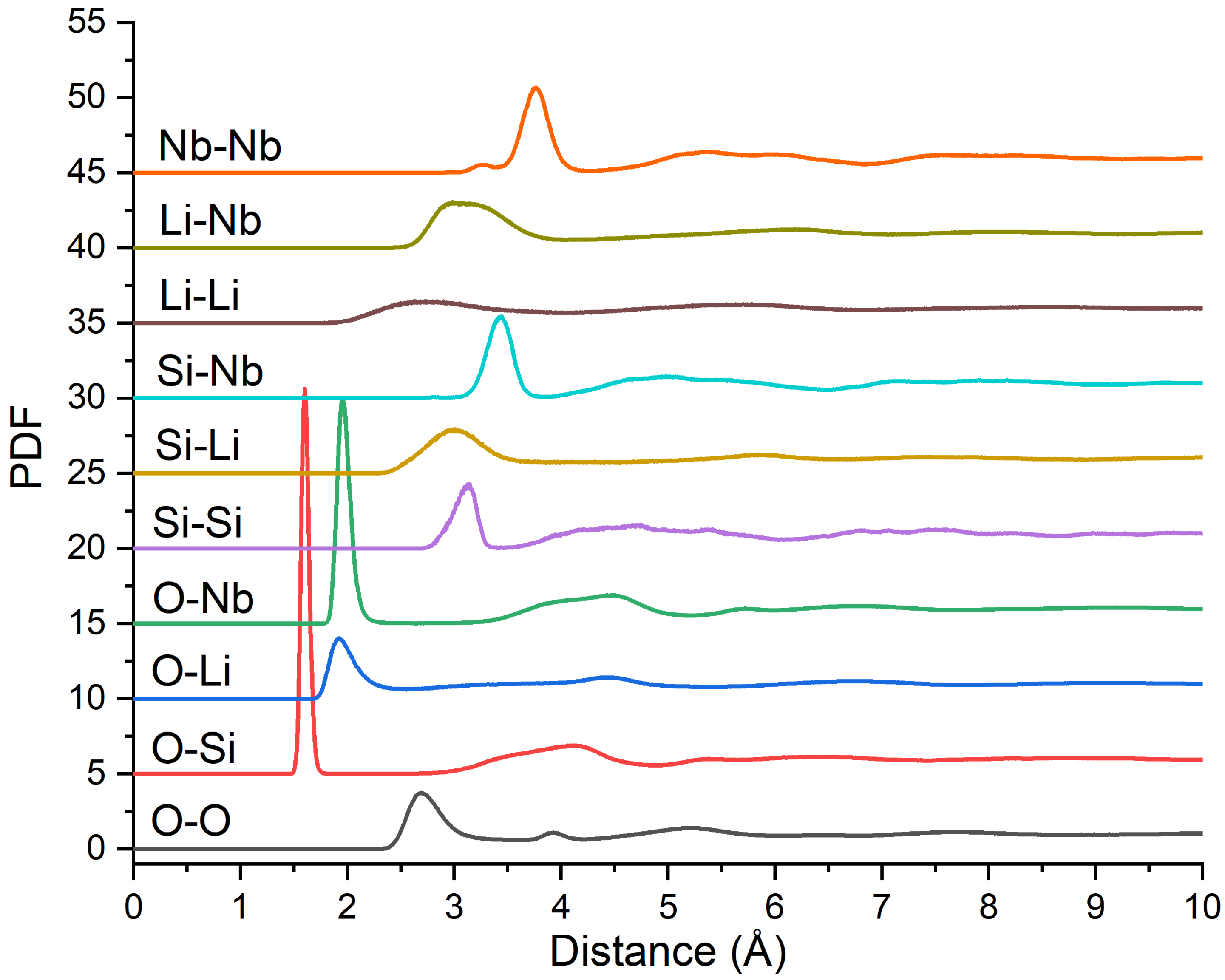

Figure 1 Pair distribution functions of pairs in simulated LNS35 glass

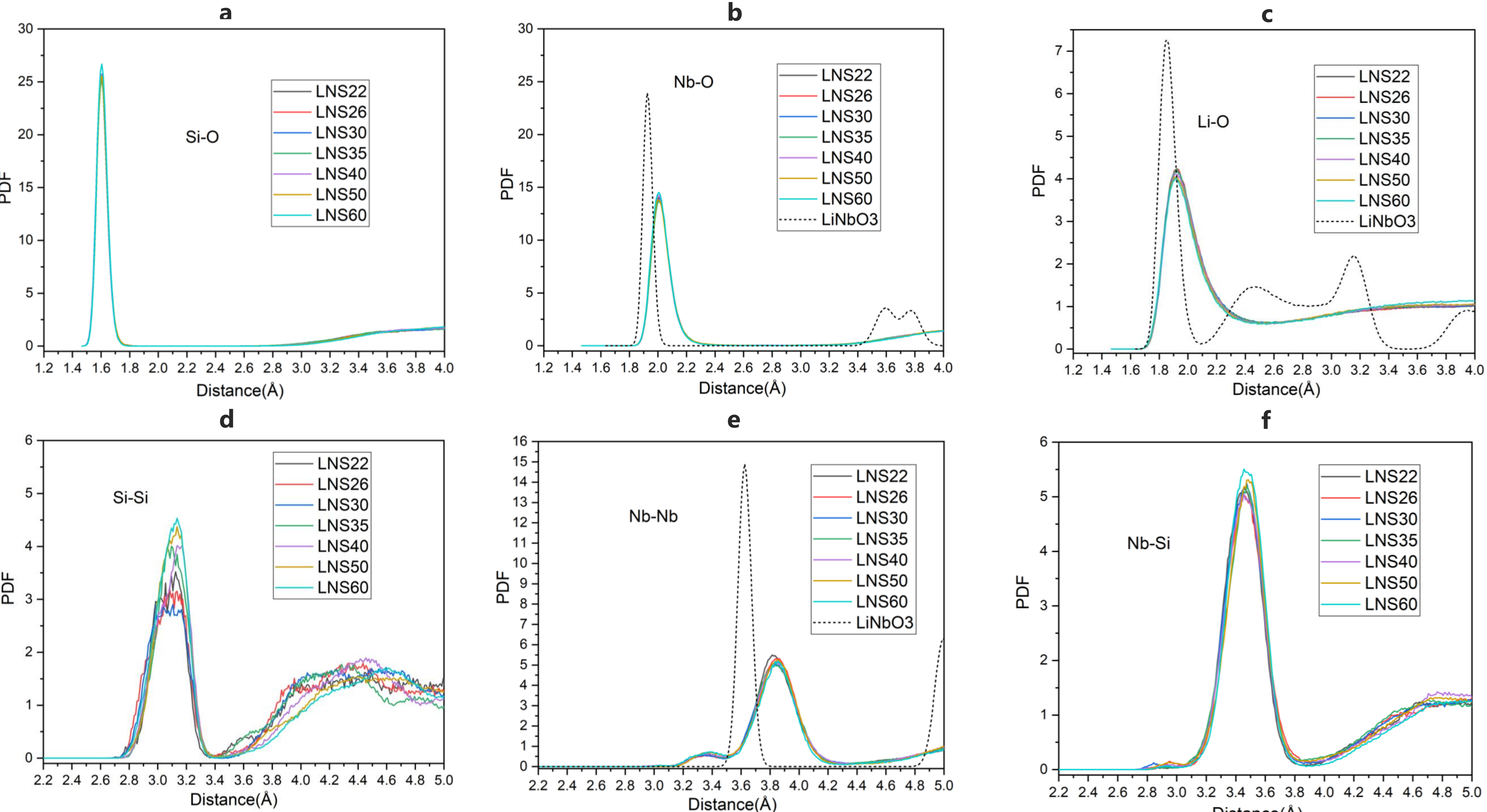

Figure 2 Pair distribution function for LNS glasses

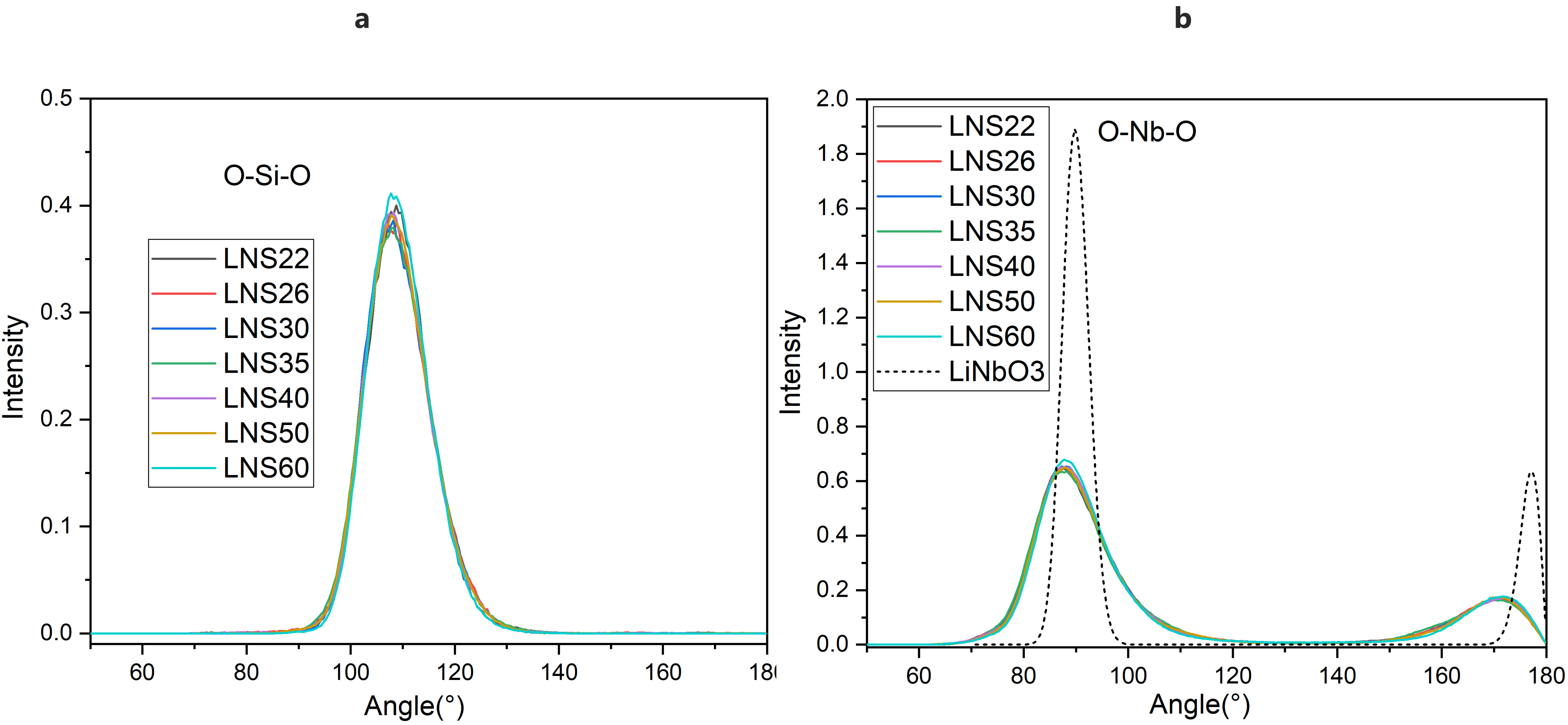

Figure 3 Bond angle distributions (BADs) of simulated LNS glasses

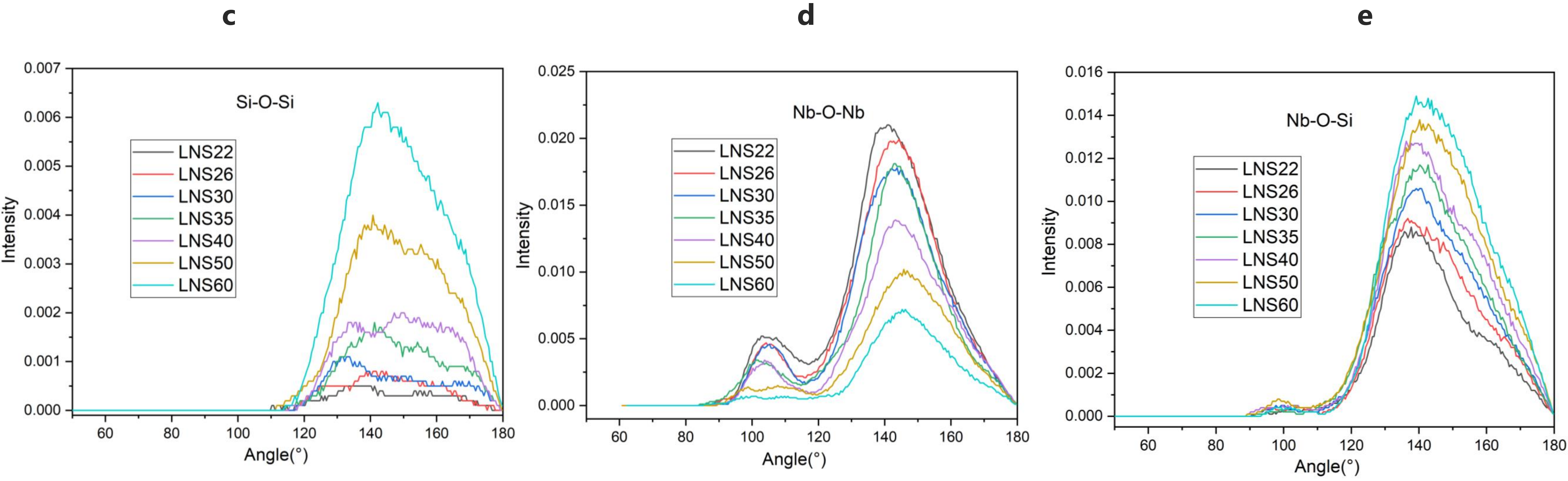
c
d
e
Si-O-Si
Nb-O-Nb
Nb-O-Si
LNS22
LNS26
LNS30
LNS35
LNS40
LNS50
LNS60
Intensity
Angle(°)

Figure 3

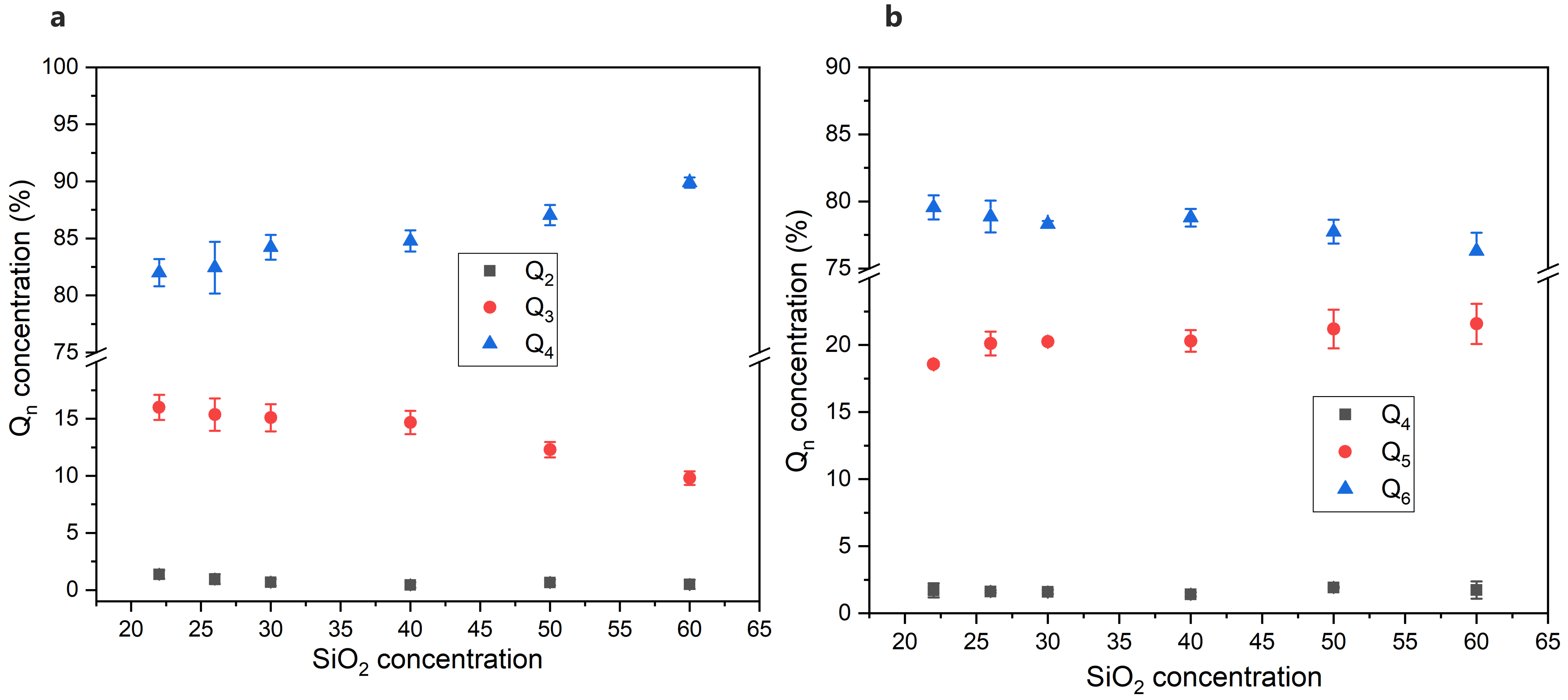

Figure 4 Q_n distribution of a, Si and b, Nb in simulated LNS glasses

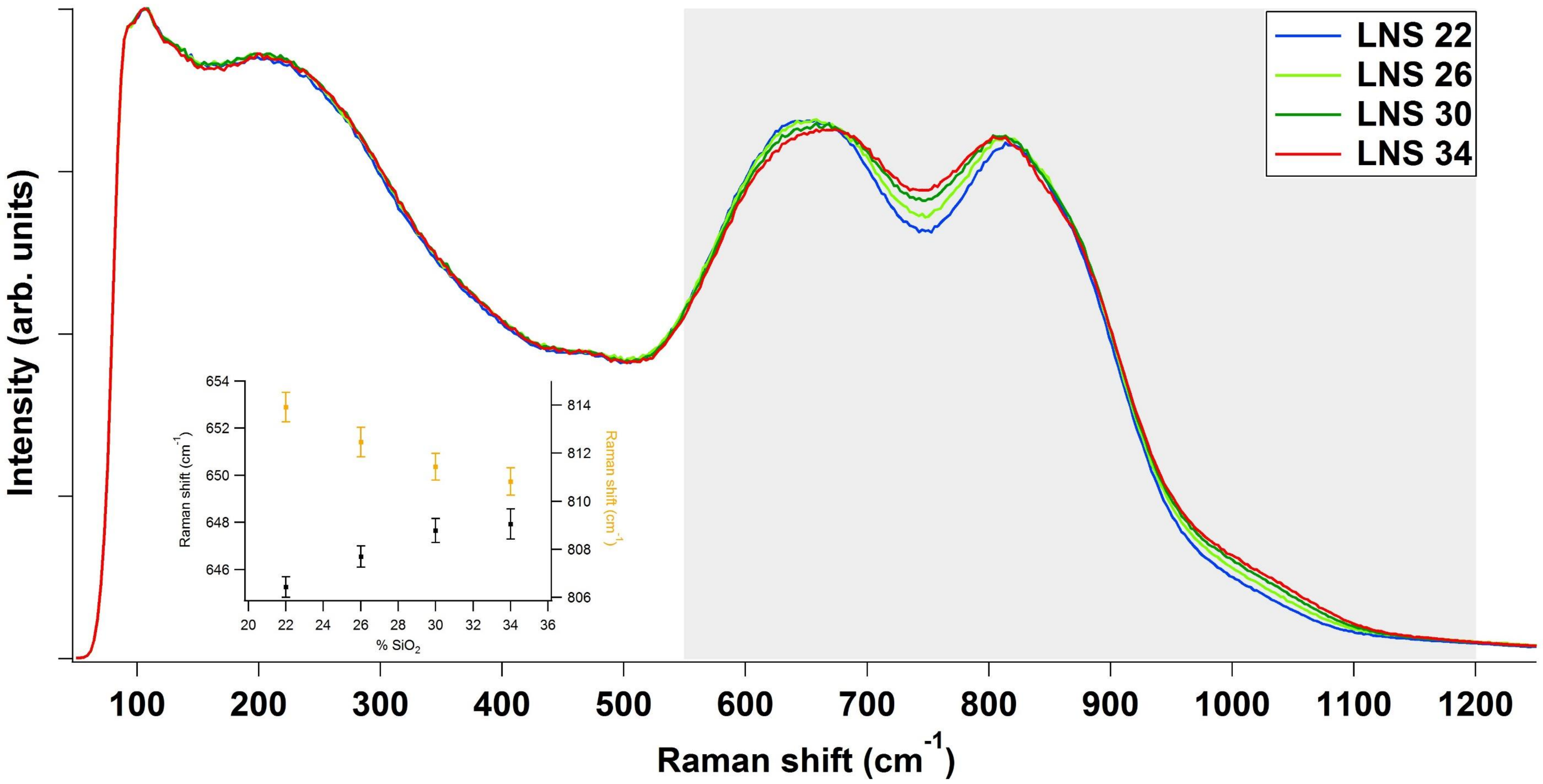

Figure 5 Raman spectra of LNS glasses. Gray region indicates the range in which fitting was performed.

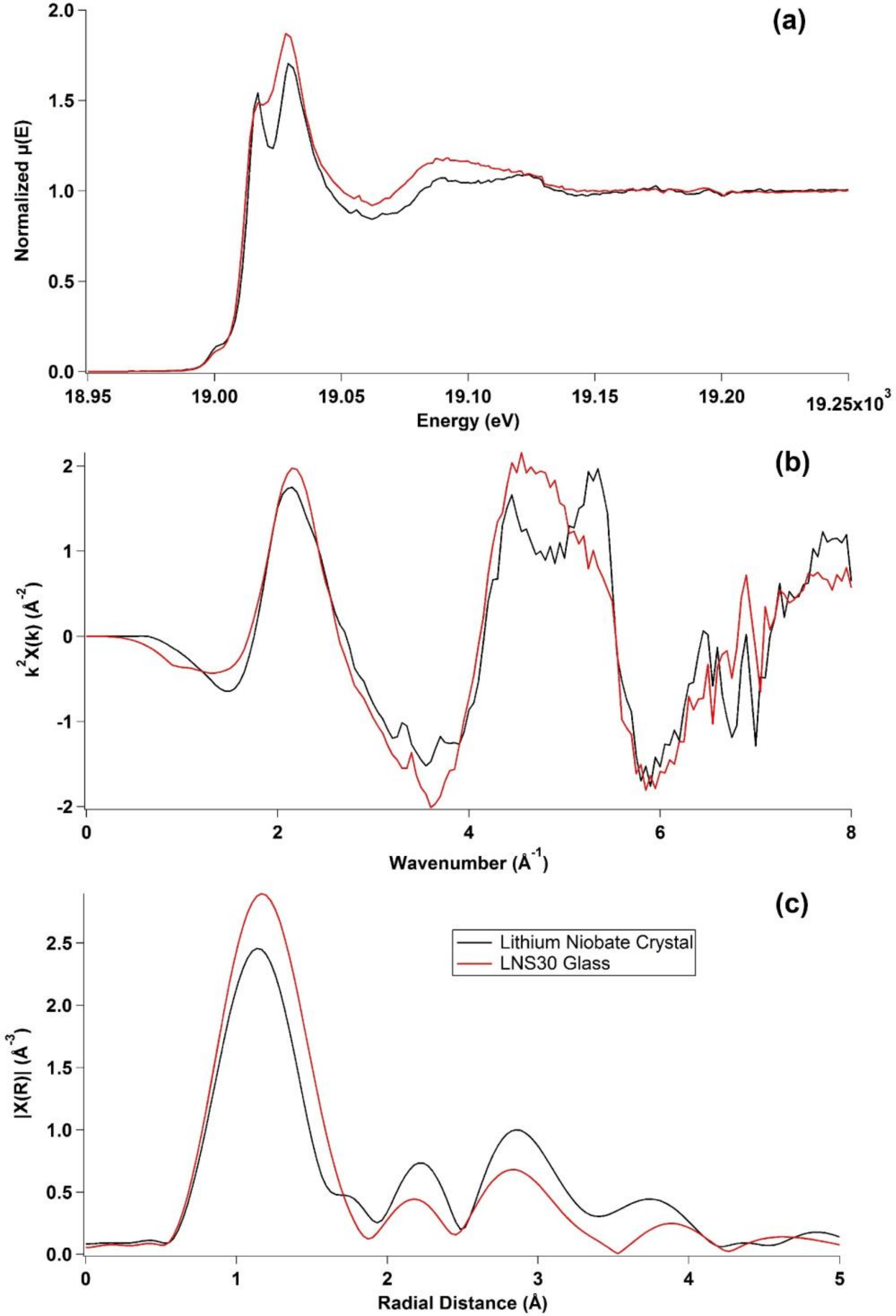

Figure 6. Nb K-edge EXAFS spectra of LNS30 glass: (a) E-space, (b) k-space, and (c) real space

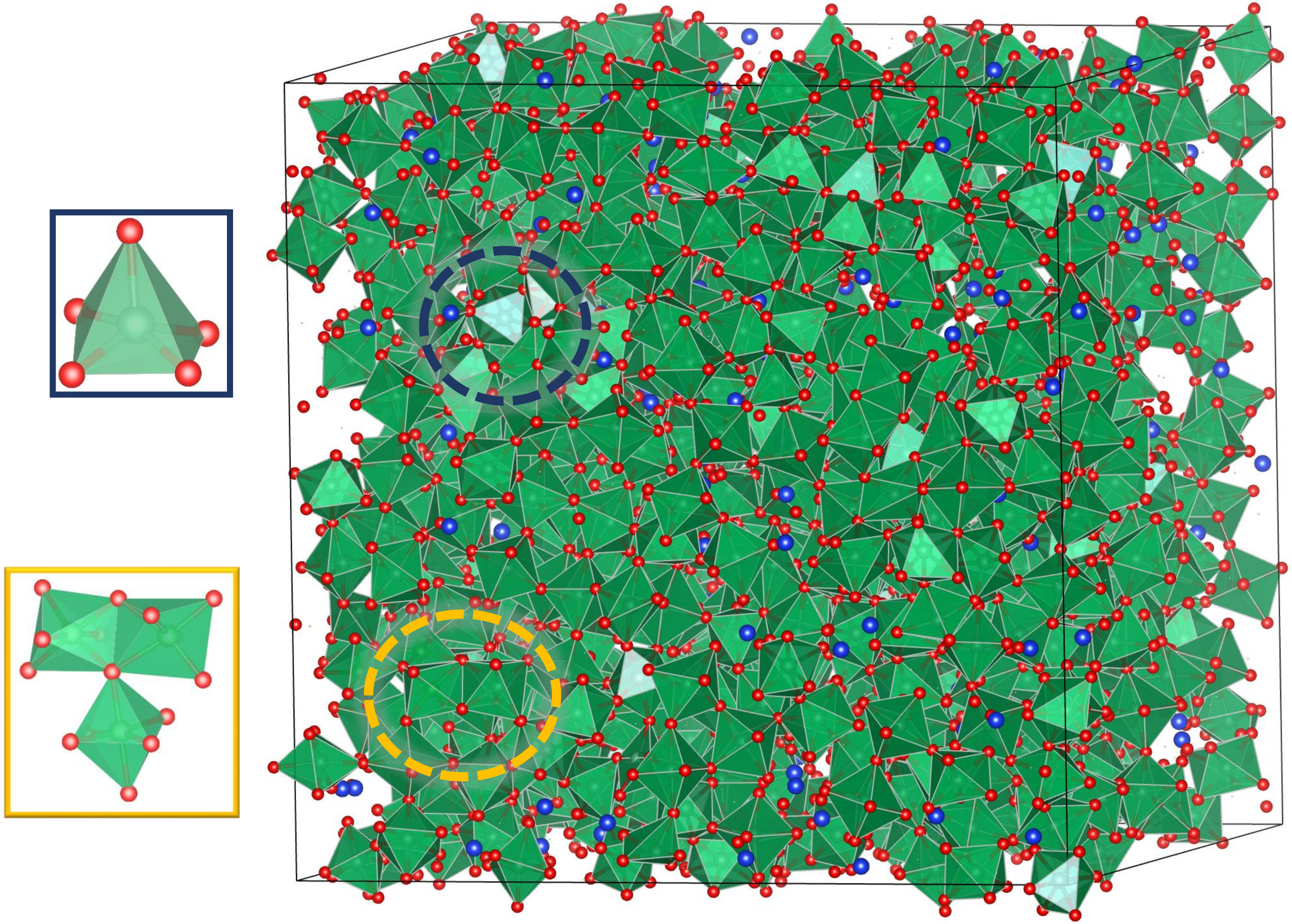

Figure 7 Schematic structures of simulated LNS22 glass (right), [NbO5] structure (top left), and TBO with edge-sharing [NbO6]-[NbO6] linkages (bottom left)